
TOWARDS MORE GENERAL VIDEO-BASED DEEPPFAKE DETECTION THROUGH FACIAL FEATURE GUIDED ADAPTATION FOR FOUNDATION MODEL

Yue-Hua Han^{1♣†}

Tai-Ming Huang^{2♣†}

Shu-Tzu Lo^{3♣†}

Po-Han Huang^{4♣†}

Kai-Lung Hua^{5♣*}

Jun-Cheng Chen^{6†}

*Microsoft

†Academia Sinica

♣National Taiwan University of Science and Technology

⁵kai.hua@microsoft.com

{³m11115q20, ⁴m11015q12}@mail.ntust.edu.tw

{¹m11015114, ²m11015114, ⁶pullpull}@citi.sinica.edu.tw

ABSTRACT

With the rise of deep learning, generative models have enabled the creation of highly realistic synthetic images, presenting challenges due to their potential misuse. While research in Deepfake detection has grown rapidly in response, many detection methods struggle with unseen Deepfakes generated by new synthesis techniques. To address this generalisation challenge, we propose a novel Deepfake detection approach by adapting the Foundation Models with rich information encoded inside, specifically using the image encoder from CLIP which has demonstrated strong zero-shot capability for downstream tasks. Inspired by the recent advances of parameter efficient fine-tuning, we propose a novel side-network-based decoder to extract spatial and temporal cues from the given video clip, with the promotion of the Facial Component Guidance (FCG) to encourage the spatial feature to include features of key facial parts for more robust and general Deepfake detection. Through extensive cross-dataset evaluations, our approach exhibits superior effectiveness in identifying unseen Deepfake samples, achieving notable performance improvement even with limited training samples and manipulation types. Our model secures an average performance enhancement of 0.9% AUROC in cross-dataset assessments comparing with state-of-the-art methods, especially a significant lead of achieving 4.4% improvement on the challenging DFDC dataset.

Keywords Deepfake Detection · CLIP · Parameter-Efficient Fine-Tuning

1 Introduction

With the advancement of deep learning technology, generative models [15, 13, 31, 10, 16, 30, 26], have enabled the general public to create highly realistic synthetic images. Such images can easily mislead viewers. In the wrong hands, they have the potential to incite social unrest and pose significant threats.

Research on Deepfake detection has surged due to the growing threat of highly realistic synthetic images. However, many methods struggle against unseen Deepfakes from new synthesis techniques [20, 9, 35, 21, 5, 45]. It’s crucial to develop models with robust generalisation capabilities that can distinguish real from Deepfake samples, especially in unfamiliar scenarios. Notable efforts include Face X-Ray[20], which detects Deepfake boundaries; LipForensic[9], emphasizing lip motions using a lip-reading pre-trained model; and SBI[35], a self-supervised learning method that blends Deepfake images with real images combining generic augmentation techniques, enhancing training efficiency and detection performance.

The rapid advancement in Foundation Model (FM) research has resulted in significant achievements in image tasks. Key contributions include the Contrastive Language–Image Pretraining (CLIP) by [29] for zero-shot image classification, the use of Self-Supervised Learning (SSL) for image segmentation and retrieval in [27], the method for zero-shot image segmentation proposed by [17], and the Diffusion Model (DM) for high-quality image generation by [30]. These FMs exhibit remarkable generalisation capabilities, consistently handling unseen samples. This consistent performance raises an intriguing question: Considering the inherent robust generalisation properties of the FMs, could they emerge as pivotal tools in the domain of Deepfake detection?

Leveraging the remarkable capabilities of Foundation Models (FMs), our research explores their utility as generalized detectors of Deepfakes. Utilizing the CLIP model, renowned for its zero-shot learning capabilities, we have formulated a Deepfake detection strategy that integrates a novel side-network decoder with layer-wise spatial and temporal modules, and the Facial Component Guidance (FCG). This guidance encourages the model to concentrate on crucial facial areas, enhancing its generalizability. Our experimental findings underscore the effectiveness of this method, showcasing cross-dataset performance that outstrips current State-Of-The-Art (SOTA) methods by an average of 0.9% in AUROC and notably achieves a significant improvement of 4.4% on the demanding DFDC dataset.

Our main contributions are summarized as follows:

- We develop a parameter-efficient fine-tuning architecture designed to decode features across both spatial and temporal dimensions, which has proven to be highly effective in enhancing generalization through extensive experiments.
- The proposed FCG mechanism can effectively boost the model’s generalisation capabilities by guiding the model to focus on important facial regions.
- Our method has shown remarkable effectiveness against unseen Deepfake samples. In our primary evaluation metric, we surpass SOTA methods and achieve an average improvement of 0.9%.

2 Related Work

In this section, we briefly review the recent relevant works on (1) Foundation Models and parameter efficient fine-tuning, and (2) Deepfake detection as follows.

2.1 Foundation Model and Parameter Efficient Fine-tuning

In modern identification and recognition tasks, large-scale FMs pre-trained on extensive and diverse data have become the new gold standard. These “FMs” are adaptable for various downstream tasks, characterized by their training on vast datasets through advanced methods, thus yielding potent feature extraction capabilities. Multi-modal techniques further enhance their rich semantic understanding. Notable examples include CLIP [29] with its robust visual-text encodings, its expanded counterpart OpenCLIP [2], the image-generating Stable Diffusion [31], and the self-supervised DINOv2 [27]. These models expedite downstream task development, as exemplified by EVL [23] and DIFT [36], which utilize foundational models for video action recognition and image correspondence, respectively.

However, adapting these models to specific tasks poses challenges, especially considering their model sizes. While full fine-tuning may be prohibitive, partial fine-tuning strategies have emerged. LoRA [10] offers an innovative approach to adapting large-scale language models. By incorporating rank decomposition matrices into the Transformer structure, LoRA substantially trims the number of trainable parameters, ensuring efficient adaptation. In [11], the authors propose Visual-Prompt Tuning (VPT) a cost-effective method for fine-tuning large-scale VisionTransformer(ViT) models. Instead of full fine-tuning, VPT employs trainable “prompt” that interface with the frozen pre-trained models, ensuring reduced training overhead. EXPRES [3] innovates to construct downstream representations by using learnable “output” tokens alongside residual learnable tokens, allowing for more effective steering of the downstream task outcomes. The SAN [25] adds a streamlined side network to the static CLIP model for open-vocabulary semantic segmentation. Deciding on the most effective adaptation method for maximizing a model’s capabilities remains a focal research point.

2.2 Deepfake Detection

The research and development of Deepfake detection have led to a wide range of methods being explored to address this issue. In the early stages of research, Xception [33] is used for classification and demonstrated good performance in intra-dataset testing. However, there is a significant drop in performance during cross-dataset evaluation. Subsequent studies focus on leveraging information that Deepfake models struggle to generate, aiming to enhance the model’s generalisation capability. FTCN [44] draws inspiration from the success of transformers in the computer vision field, utilizing 3D Convolution and transformer architecture to detect temporal anomalies. LipsForensics [9] and EyesTellAll [7] target at irregular lip and pupil shapes respectively, aiming to exploit weaknesses in Deepfake models. With the evolution of self-supervised learning techniques, recent studies [35, 20, 1, 43] have incorporated self-supervised learning to synthesize Deepfake samples, addressing the issue of insufficient training dataset diversity. Beyond image-based self-supervised learning, RealForensics [8] pre-trains the backbone on lip-reading datasets and further optimizes the performance through performing self-supervised learning by exploiting audio and image consistency. AltFreezing [41] proposes a strategy that alternately freezes spatial and temporal weights of a network during training. Finally, TALL-Swin [42] introduces a novel approach to Deepfake

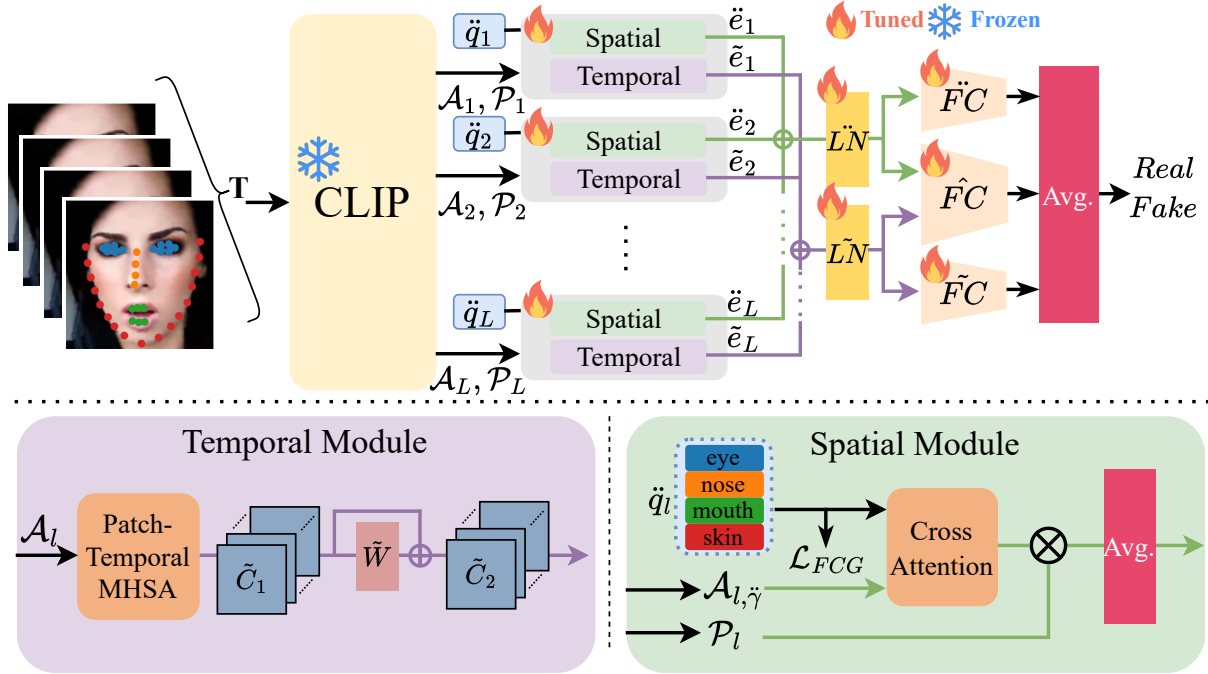


Figure 1: **Framework Overview:** Our method utilizes the CLIP image encoder to extract layer-wise features, which are then processed by the corresponding decoder block consist of temporal and spatial modules for parameter-efficient tuning. The temporal module exploits the Patch-Temporal Multi-Head Self-Attention and a residual projection layer to capture the temporal inconsistency of Deepfake videos. The spatial module incorporates the FCG loss to compile a comprehensive representation from key facial part in every frame of the video clip. Ultimately, our framework aggregates the outputs of all spatial and temporal modules for the final prediction, where the mathematical accent notations of \tilde{x} , \hat{x} , and \tilde{x} represent temporal related, spatial related, spatio-temporal related components, respectively.

video detection by transforming video clips into predefined layouts to efficiently preserve spatial and temporal dependencies.

3 Method

Our approach focuses on harnessing the inherent capabilities of foundation models to identify temporal inconsistencies and spatial manipulations in Deepfake videos. To this end, we have developed a framework that leverages the rich representation of the pre-trained foundation model (i.e., CLIP) and integrates a side-network decoding block, comprising both specialized temporal and spatial modules, to capture these key characteristics for Deepfake detection as illustrated in Fig. 1. The following section first outlines the model’s overall architecture (Section 3.1) before delving into the details of the proposed multi-layer temporal (Section 3.2) and spatial modules (Section 3.3).

3.1 Overall Framework

Drawing inspiration from the works of [23, 24], we utilize the ViT-based image encoder of a foundational model—specifically, the CLIP image encoder—to extract versatile features that our side-network spatial and temporal modules can use for Deepfake video detection. To facilitate understanding of the proposed method, we first introduce several symbols and notations representing the system configuration: L denotes the number of transformer layers, P the number of patches, T

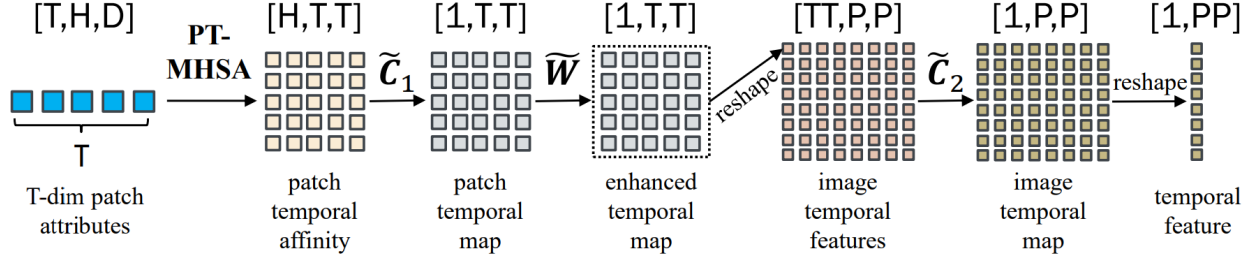


Figure 2: **Illustration of the Temporal Module Mechanism:** For enhanced clarity, we present a step-by-step demonstration of the operation within the temporal module. This example considers only a single attribute, that is $|\tilde{\Gamma}| = 1$. For scenarios involving multiple attributes, simply multiply H by the number of selected attributes.

the number of input frames, H the number of attention heads in multi-head self-attention, and D the feature dimension per head. In addition, **we follow the convention in the rest of the paper that the mathematical accent notations of \tilde{x} , \tilde{x} , and \hat{x} represent temporal related, spatial related, spatio-temporal related components respectively.**

For each transformer layer of the image encoder, we initially obtain patch embeddings $\mathcal{P}_l \in \mathbb{R}^{T \times P \times (H \times D)}$ and attention attributes $\mathcal{A}_{l,\gamma} \in \mathbb{R}^{T \times P \times H \times D}$, where $1 \leq l \leq L$ indicates the layer index, and $\gamma \in \{q, k, v\}$ specifies the attention attribute type (i.e., query, key and value). Further details on attribute extraction are available in the supplementary materials. These attributes are then processed by a layer-specific decoder block and analyzed by the respective spatial and temporal modules, resulting in temporal and spatial embeddings \tilde{e}_l and \tilde{e}_l for each layer. We aggregate these layer-specific embeddings to form comprehensive representations, denoted as \tilde{E} and \tilde{E} , which are subsequently normalized using respective LayerNorm layers \tilde{LN} and \tilde{LN} . The framework employs three independent classification heads (\tilde{FC} , \tilde{FC} , and \tilde{FC}), which are realized by a respective fully connected (FC) layer for temporal, spatial, and spatio-temporal branches, to predict Deepfake levels and a combined Deepfake presence, with the final score being the average of these heads' outputs during inference.

3.2 Temporal Module

In the l -th decoder block, our temporal module focuses on capturing the temporal continuity of patch locations. We accomplish this by selecting certain attributes $\tilde{\Gamma} \subseteq \{q, k, v\}$ from \mathcal{A}_l of the l -th encoder layer.

Initially, for each fixed patch location, we apply Multi-Head Self-Attention (MHSA) across the temporal axis, which we dubbed as the Patch-Temporal Multi-Head Self-Attention (PT-MHSA), for each chosen attribute in $\tilde{\Gamma}$. This generates a temporal affinity map $\tilde{\mathcal{M}}_1 \in \mathbb{R}^{P \times (|\tilde{\Gamma}| \times H) \times T \times T}$, applying a softmax function on its last axis to normalize affinities. Next, we compress the multi-head affinity scores at adjacent time points and integrate them using a 2D kernel $\tilde{\mathcal{C}}_1$ that convolves over $\tilde{\mathcal{M}}_1$'s last two dimensions, yielding another feature map $\tilde{\mathcal{M}}_2 \in \mathbb{R}^{P \times 1 \times T' \times T'}$. This map is then processed through a residual layer $\tilde{\mathcal{W}}$ to produce $\tilde{\mathcal{M}}_3$ with the same shape as $\tilde{\mathcal{M}}_2$, where $\tilde{\mathcal{W}}$ consists of two FC layers and a ReLU activation layer in-between and is used to promote the interaction of temporal representations across all $T' \times T'$ time points for better capturing the temporal nuances of the video.

To incorporate spatially adjacent patch information, we reshape $\tilde{\mathcal{M}}_3$ into $(T' \times T') \times \sqrt{P} \times \sqrt{P}$ and apply a 2D convolution using kernel $\tilde{\mathcal{C}}_2$ on the last two dimensions, resulting in the aggregated

feature $\tilde{\mathcal{M}}_4 \in \mathbb{R}^{1 \times \sqrt{P} \times \sqrt{P}}$. Finally, we further reshape $\tilde{\mathcal{M}}_4$ into $\tilde{e}_l \in \mathbb{R}^{P \times 1}$ as the temporal feature for the l -th decoder layer. We also illustrate the whole process in Fig. 2.

3.3 Spatial Module

The spatial module in our decoder is designed to extract and utilize cues from the generalizable features of image patches \mathcal{P}_l . In the following, we first introduce the pipeline of spatial module, explain how we identify layer-wise attributes associated with each major facial component through facial attribute mining, and discuss the details of the proposed FCG loss which empolys contrastive objective function to align the per-layer queries with the identified facial attributes. The FCG is used to enhance the generalizability of the spatial module and avoid overfitting to dataset-specific characteristics by guiding it towards focusing on key facial features during the optimization process, namely, lips, skin, eyes, and nose.

Pipeline. Starting with N learnable queries, denoted as $\tilde{q}_l \in \mathbb{R}^{N \times (H \times D)}$, we employ Cross-Attention (CA) across the selected attribute $\tilde{\gamma}$ of all video patches to produce an affinity map $\tilde{\mathcal{M}}_1 \in \mathbb{R}^{T \times N \times P}$, where $\tilde{\mathcal{M}}_1 = \mathbf{CA}(\tilde{q}_l, \mathcal{A}_{l, \tilde{\gamma}})$. We then combine per-query affinity maps with the patch embeddings \mathcal{P}_l from the l -th encoder layer to obtain the query feature map $\tilde{\mathcal{M}}_2 \in \mathbb{R}^{T \times N \times (H \times D)}$. The final step involves averaging over the first two dimensions to produce the layer-specific spatial feature $\tilde{e}_l \in \mathbb{R}^{(H \times D) \times 1}$.

Facial Attribute Mining. Before computing FCG loss, we first identify layer-specific attributes associated with key facial parts (lips, skin, eyes, nose) to guide the spatial module’s per-layer queries \tilde{q}_l during training. We start by selecting several frames from pre-processed, facially aligned videos. These frames undergo various random augmentations such as resizing, cropping, and bidirectional flipping. After augmentation, these frames are inputted into the CLIP image encoder to extract the layer-wise $\tilde{\gamma}$ attributes $\mathcal{A}_{l, \tilde{\gamma}}$. Utilizing landmark coordinates from the preprocessing phase allows us to pinpoint patch locations for each facial parts. We then aggregate patch attributes corresponding to each facial parts from $\mathcal{A}_{l, \tilde{\gamma}}$, and average them after L_2 -normalization, resulting in layer-wise facial part attributes $\tilde{\varphi}_l \in \mathbb{R}^{4 \times (H \times D)}$, where the first dimension is aligned with lips, skin, eyes, and nose, respectively. The augmentation step is critical to ensure the model does not retain spatially dependent cues in its attention attributes.

Facial Component Guidance. Once finishing facial attribute mining, we then adopt the InfoNCE loss function to compute the FCG loss which encourages \tilde{q}_l to closely match their respective facial component attribute in $\tilde{\varphi}_l$. The FCG loss is calculated as per Equation 1:

$$\mathcal{L}_{FCG} = \frac{1}{NL} \sum_{l=1}^L \left(\sum_{i=1}^N \log \left(\frac{\exp(\mathbf{cos}(\tilde{q}_{l,i}, \tilde{\varphi}_{l,i}) \times \tau)}{\sum_{j=1}^N \exp(\mathbf{cos}(\tilde{q}_{l,i}, \tilde{\varphi}_{l,j}) \times \tau)} \right) \right), \quad (1)$$

where τ denotes the softmax temperature, $N = 4$ the number of facial parts, and \mathbf{cos} stands for the cosine similarity between two vectors. The number of queries is equal to that of facial parts.

3.4 Objective Functions

The primary objective function comprises the focal loss [22] $\mathcal{L}_F(\cdot)$ derived from the three distinct classification heads for temporal (\mathcal{L}_T), spatial (\mathcal{L}_S), and spatio-temporal branches (\mathcal{L}_{ST}) respectively:

$$\mathcal{L}_T = \mathcal{L}_F(\tilde{\mathbf{F}}\mathbf{C}(\tilde{\mathbf{L}}\tilde{\mathbf{N}}(\tilde{E})), y), \quad (2)$$

$$\mathcal{L}_S = \mathcal{L}_F(\ddot{\mathbf{F}}\mathbf{C}(\ddot{\mathbf{L}}\ddot{\mathbf{N}}(\ddot{E})), y), \quad (3)$$

$$\mathcal{L}_{ST} = \mathcal{L}_F(\hat{\mathbf{F}}\mathbf{C}(\mathit{cat}(\tilde{\mathbf{L}}\tilde{\mathbf{N}}(\tilde{E}), \ddot{\mathbf{L}}\ddot{\mathbf{N}}(\ddot{E}))), y), \quad (4)$$

where $\mathit{cat}(\cdot)$ represents the concatenation operation that merges the provided features and y is the ground truth label in either real or fake. The total objective for training the model is defined as:

$$\mathcal{L}_{total} = \mathcal{L}_T + \mathcal{L}_S + \mathcal{L}_{ST} + w\mathcal{L}_{FCG}, \quad (5)$$

where w adjusting the influence of the FCG loss on the overall training objective.

4 Experiments

In this section, we first introduce the evaluation setup and implementation details followed by extensive evaluation results on different Deepfake detection benchmark datasets and ablation studies.

4.1 Implementation Details

Unless stated, we base our method on the CLIP ViT-L/14¹ image encoder which includes 24 encoder layers ($L = 24$). In our preprocessing approach, we adopt RealForensics’ method by using the 2D-FAN² tool to extract landmarks from video frames, aligning them with the mean face from the LRW dataset before cropping. We improve facial tracking stability by examining landmark distances between consecutive frames. During training, non-overlapping clips ranging 2 to 4 seconds are randomly extracted from each video, 10 frames are then uniformly sampled ($T = 10$) from the extracted clips. The sampled frames are processed through our video-level augmentation pipeline, including: horizontal flipping, random resizing and cropping, RGB shifting, hue and saturation adjustments, random modifications to brightness and contrast, image compression, blurring, and downscaling. This diverse augmentation strategy is designed to simulate a wide range of real-world variations. Our training process spans 30 epochs on a setup with $4 \times$ V100 GPUs, accommodating a batch size of 240 clips, and concludes in approximately 3.5 hours (14 GPU hours). To optimize training, we implement an early stopping strategy, monitoring the validation subset’s Area Under the Receiver Operating Characteristic (AUROC) score with a patience of 10 epochs.

In the spatial module, we set the $\tilde{\gamma}$ parameter to primarily focus on the k attribute. For the temporal module, the convolution kernels \tilde{C}_1 and \tilde{C}_2 are configured with a kernel size of 5, padding of 2, and a stride of 1. The optimization employs the AdamW optimizer, setting the learning rate (lr) to $1e-3$, with β parameters at $(0.9, 0.999)$, and a weight decay of $1e-4$. The loss function weight (w) is adjusted to 0.15. We utilize focal loss for classification, with a gamma value of 4 to focus on challenging samples. Our methodology also incorporates half-precision computing techniques. For evaluation, we adhere to the protocols outlined by RealForensics, focusing on reporting the video-level AUROC in percentage. This assessment specifically involves models trained on the High Quality (HQ) subset of the FaceForensics++ (FF++) [33] dataset.

¹<https://github.com/openai/CLIP>

²<https://github.com/ladrianb/face-alignment>

4.2 Evaluation Datasets for Deepfake Detection

We introduce the Deepfake datasets employed in our experiments as follows: The **FaceForensics++ (FF++)** dataset, introduced by [33], consists of 1,000 real videos and 4,000 Deepfake videos. These Deepfake videos are created using two face-swapping techniques—Deepfake [4] and FaceSwap [18]—and two face reenactment methods, NeuralTexture [37] and Face2Face [38]. Unless otherwise stated, we utilize the moderately compressed version (c23) of this dataset. The **CelebDF-v2 (CDF)** dataset, proposed by [21], includes 5,639 high-quality DeepFake videos of celebrities created using an advanced synthesis process. Our experiments utilize the test split of this dataset, which contains 518 testing videos. The **Deep Fake Detection Competition (DFDC)** dataset, from [5], is a large-scale dataset with 124,000 videos, where Deepfake videos are created using 8 different algorithms. We evaluate a subset of 3,215 videos from the test split, in line with the Realforensics approach. **FaceShifter (FSh)**, an occlusion-aware face swapping algorithm introduced by [19], produces high-fidelity videos. Lastly, [12] introduced the **DeeperForensics (DFo)** dataset featuring 60,000 videos and 17.6 million frames. This dataset is enhanced with real-world perturbations to increase its diversity and challenge. Since both the FSh and DFo datasets generate their content using real videos from FF++, we employ the test split of the FF++ dataset for evaluation purposes.

4.3 Generalisation to Unseen Dataset

In Table 1, we assess the generalization capability of our model, trained on the FaceForensics++ (FF++) dataset, against four unseen datasets: CDF, DFDC, FSh, and DFo. To provide a comparative analysis, we include scores from previous methods as reported in their respective papers and official repositories. As a baseline, we utilize linear probe techniques on two CLIP image encoders, ViT-L/14 and ViT-B/16, to establish a fundamental point of comparison. Such probing models, without additional constraints, might lean towards dataset-specific cues, compromising generalizability. Despite this, CLIP’s image encoders’ innate generalizability is evident, significantly outperforming the Face X-ray method.

By integrating CLIP’s robust generalizability with our proposed method, we observe a notable improvement in performance across both ViT architectures. Specifically, our approach using the ViT-L/14 encoder outperforms the SOTA by an average of 0.9% AUROC. This improvement is particularly pronounced in the challenging DFDC dataset, where our method establishes a significant lead of 4.4% AUROC. These results underscore the effectiveness of combining CLIP’s generalizable features with our model’s architecture, thereby enhancing performance across diverse Deepfake detection scenarios.

4.4 Ablation Study on Model Components

In Table 2, we evaluate the contribution of various components to the model’s ability to generalize across different datasets. Our findings highlight the crucial role of our dual-module architecture; removing either the spatial or temporal module results in a performance decline of over 4.5%. Notably, excluding the spatial module significantly impacts performance on the challenging CDF and DFDC datasets. This underscores the importance of semantic learning in accurately assessing video authenticity within these datasets. Similarly, omitting the temporal module leads to a marked decrease in performance on the FSh dataset, indicating a reliance on temporal inconsistency artifacts

Table 1: **Evaluation on Cross-Datasets:** We evaluate the video-level performance of CDF, DFDC, FSh and DFo after training on the FF++ dataset to examine the generalisation ability to unseen datasets. Values in **bold** represent the best results, while those underlined indicate the second-best values.

Model	CDF	DFDC	FSh	DFo	Avg.
Xception [33]	73.7	70.9	72.0	84.5	75.3
Face X-ray [20]	79.5	65.5	92.8	86.8	81.2
LipForensics [9]	82.4	73.5	97.1	97.6	87.7
SBI(c23) [35]	92.9	72.0	-	-	-
FTCN [44]	86.9	74.0	98.8	98.8	89.6
RealForensics [8]	86.9	75.9	99.7	99.3	90.5
AltFreezing [41]	89.5	-	<u>99.4</u>	99.3	-
TALL-Swin [42]	90.8	76.8	99.7	99.6	<u>91.7</u>
linear probe(ViT-B/16)	81.7	<u>77.3</u>	73.8	93.8	81.7
Ours (ViT-B/16)	83.2	75.6	90.1	94.6	85.9
linear probe(ViT-L/14)	73.3	77.0	85.2	93.4	82.2
Ours (ViT-L/14)	<u>92.3</u>	81.2	97.5	<u>99.4</u>	92.6

Table 2: **Ablation of Model Components:** The components we consider include the spatial and temporal modules within the decoder block, the focal loss and the FCG loss. As we move from the top to the bottom of the table, each row represents a model that removes the specified component.

Comp.	CDF	DFDC	FSh	DFo	Avg.
Ours	92.3	81.2	97.5	99.2	92.6
w/o T mod.	88.4	<u>80.8</u>	82.4	98.0	87.4(-4.8)
w/o S mod.	82.4	74.5	95.6	98.6	87.8(-4.6)
w/o focal	85.8	79.1	<u>97.2</u>	98.7	90.2(-2.4)
w/o FCG	<u>88.8</u>	81.2	96.1	<u>99.1</u>	<u>91.3</u> (-1.3)

within this dataset. Therefore, our approach, which addresses unseen datasets from two distinct perspectives, proves effective in enhancing generalization.

Further analysis reveals the superiority of focal loss over traditional cross-entropy loss, with the former showing a notable improvement in handling hard samples, thereby boosting the model’s generalization capabilities. Additionally, our proposed Facial Component Guidance (FCG) enhances generalization by directing the layer-wise queries to concentrate on essential facial features. The integration of these components collectively results in a significant boost in the model’s overall performance, demonstrating the effectiveness of our design in achieving superior generalization across diverse datasets.

4.5 Analysis on Hyper-Parameters

Selection of $\tilde{\gamma}$ in the Spatial Module. In Table 3, we explore different $\tilde{\gamma}$ settings to evaluate the effectiveness of attributes to improve model generalizability to focus on major facial parts with the affinity map. We can see in the table that selecting k and q both performs well in improving generalizability while v have a degraded performance. We surmise this due to the natural design of q and k in the attention block for affinity, while v wasn’t designed for this purpose. In our experiments, we set $\tilde{\gamma} = k$ due to its slightly advanced performance.

Table 3: **Evaluation of $\tilde{\gamma}$ Parameter:** We select different $\tilde{\gamma}$ values in $\{q, k, v\}$ to evaluate the efficacy for attributes to collect informative facial features.

$\tilde{\gamma}$	CDF	DFDC	FSh	DFo	Avg.
$\tilde{\gamma} = k$	92.3	<u>81.2</u>	97.5	99.4	92.6
$\tilde{\gamma} = q$	<u>91.5</u>	81.6	<u>97.4</u>	99.4	<u>92.5</u>
$\tilde{\gamma} = v$	89.2	80.7	96.1	<u>99.1</u>	91.3

Table 4: **Evaluation on $\tilde{\Gamma}$ Parameter:** We select different $\tilde{\gamma}$ values in $\{q, k, v\}$ to evaluate the efficacy for attributes to collect informative facial features.

q	k	v	CDF	DFDC	FSh	DFo	Avg.
✓	✓	✓	92.3	<u>81.2</u>	97.5	99.4	92.6
✓	✓		88.3	79.7	96.7	<u>99.3</u>	91.0
	✓	✓	<u>90.0</u>	81.0	96.6	<u>99.3</u>	<u>91.7</u>
✓		✓	89.6	80.1	<u>97.4</u>	99.2	91.6
✓			89.7	81.1	<u>94.7</u>	98.6	91.0
	✓		88.5	81.1	94.5	99.0	90.8
		✓	89.3	81.4	95.5	99.0	91.3

Attributes within $\tilde{\Gamma}$ in the Temporal Module. In this section, we delve into the impact of varying attribute selections $\tilde{\Gamma}$, utilized by the Patch-Temporal Multi-Head Self-Attention (PT-MHSA), on the model’s generalization capabilities. We explore all possible combinations of the available attributes and document their cross-dataset performance in Table 4. Initial observations reveal that selecting any single attribute results in roughly equivalent average performance across datasets. However, when the attribute selection expands to include two attributes, we notice a slight improvement in average performance, attributed primarily to enhanced results on the FSh dataset. Optimal performance is attained upon integrating all attributes, signifying peak generalization.

This outcome suggests that the \tilde{C}_1 kernel’s ability to aggregate affinity scores across all attribute heads plays a pivotal role in this enhanced performance. It indicates that continuity cues from different heads and attributes can be complementary, contributing collectively to the model’s improved ability to generalize. This discovery highlights the capacity to leverage patch-wise continuity information for detecting jittering or motion within videos.

4.6 Data-Efficiency Evaluations

We further assess the generalizability of our proposed method trained on the FF++ dataset with additional training constraints, such as excluding certain types of manipulations and limiting the ratio of samples within the dataset. These constraints are proposed to analyse the data-efficacy characteristic of our proposed method with the generalizable features from the CLIP image encoder.

Constraint on Manipulation Types. We evaluate our method’s ability to generalize to unseen manipulation types within the FaceForensics++ (FF++) dataset by following the Leave-One-Out (LOO) scenario protocols. This method assesses the model’s performance on each manipulation type in FF++ after training on the other three types. The outcomes of this evaluation are showcased in the FF++ column of Table 5. Additionally, we extend our evaluation to cross-dataset scenarios to examine how well models trained under LOO conditions generalize towards unseen datasets.

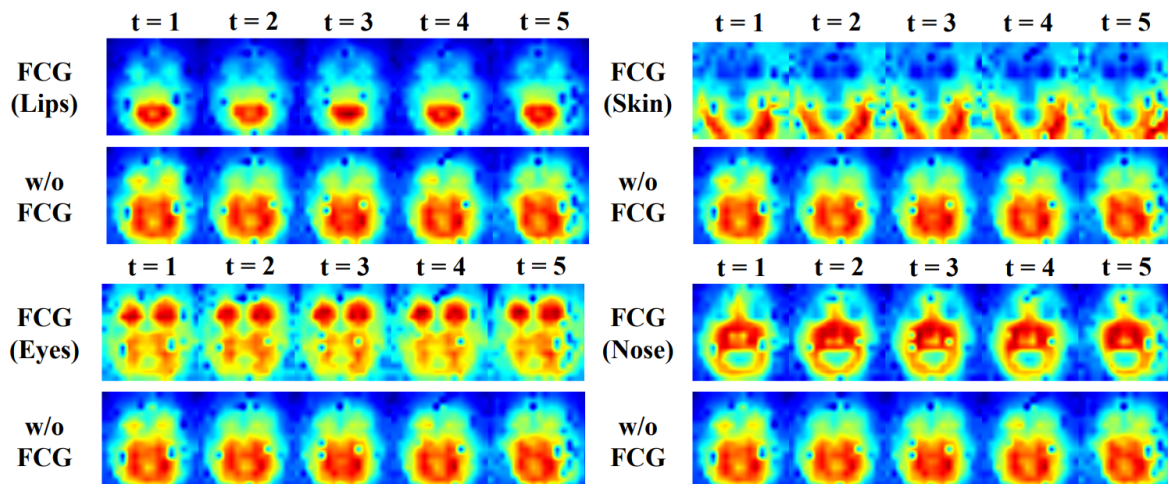


Figure 3: **Attention Visualization:** We visualize the affinity map in two settings to examine the impact of the FCG on the locations that the spatial module depends on for its predictions.

Table 5: **Generalizability under FF++ Leave-One-Out (LOO):** In this analysis, we explore the model’s performance under the conventional LOO cross-manipulation setting, alongside its corresponding cross-dataset generalization capabilities. The top-performing scores in each LOO are highlighted in **bold**. For cross-dataset evaluations, we utilize the LOO weights made available by RealForensics.

w/o	Model	FF++	CDF	DFDC	FSh	DFo	Avg.
DF	RealForensics	100.0	69.2	72.4	90.5	99.2	82.8
	Ours	99.4	90.8	78.6	96.3	98.8	91.1
FS	RealForensics	97.1	80.0	71.2	98.5	99.4	87.3
	Ours	92.9	89.5	76.3	94.6	98.7	89.8
F2F	RealForensics	99.7	75.7	72.3	99.1	99.9	86.9
	Ours	99.4	92.0	82.1	97.5	99.0	92.7
NT	RealForensics	99.2	80.8	72.4	93.8	98.6	87.8
	Ours	92.4	87.3	82.4	94.4	99.0	90.8

In the LOO evaluations, RealForensics achieves slightly higher performance than our method on the NT and FS manipulations. However, for cross-dataset evaluations, RealForensics experiences notable performance declines across all LOO scenarios. Conversely, our approach consistently demonstrates superior performance on the challenging CDF and DFDC datasets and maintains parity with RealForensics on the FSh and DFo datasets. This indicates our method’s enhanced capability to generalize across unseen datasets, even when trained on a limited selection of known manipulation types. Furthermore, we suggest that RealForensics may be biased towards dataset-specific cues for Deepfake detection. This is inferred from its consistent performance on the FF++-family datasets (FSh and DFo), coupled with notable performance declines when faced with completely unseen datasets (CDF, DFDC).

Constraint on Dataset Samples. In this experiment, we focus on another dimension of data scarcity: the limited number of Deepfake samples. Our objective is to assess our model’s capacity to generalize across varying amounts of training samples. The findings are detailed in Table 6, where we train our model using different proportions of the FF++ training dataset and subsequently conduct cross-dataset evaluations. Remarkably, our method demonstrates robust performance,

Table 6: **Generalizability on Proportional Training Dataset:** To further validate the efficacy of our approach, we assess the generalizability of our model when trained on varying proportions of the training dataset. This evaluation aims to showcase the model’s performance under scenarios with limited training samples.

portion	CDF	DFDC	FSh	DFo	Avg.
10%	73.7	70.9	89.4	98.0	83.0
25%	88.7	75.8	93.8	98.8	89.3
50%	88.6	79.1	96.2	98.8	90.7
75%	<u>91.1</u>	<u>80.2</u>	97.7	<u>99.3</u>	<u>92.1</u>
100%	92.3	81.2	<u>97.5</u>	99.4	92.6

Table 7: **Unseen Face Domain Evaluation:** We further evaluate the zero-shot detection performance in AP(%) across diffusion models. * denotes the detectors are further trained on CelebA-HQ [14] split of the DiffusionForensics [40] dataset.

Method	Generated face images				Avg.
	SD-v2	IF	DALLE-2	Midjourney	
SBI [35]	70.8	83.9	64.4	41.5	65.2
Ours	99.2	95.8	87.5	86.2	92.2
CNNDet* [39]	<u>99.8</u>	82.7	33.7	69.3	71.4
F3Net* [28]	99.1	84.9	69.8	<u>87.9</u>	<u>85.4</u>
DIRE* [40]	100	<u>99.9</u>	99.9	100	100
Ours*	100	100	<u>99.3</u>	100	100

showing no significant loss with just 75% of the dataset. Furthermore, it outperforms RealForensics when trained on only 50% of the dataset. This enhanced performance can be attributed to our strategy of leveraging a foundational model combined with an approach designed to retain strong generalization capabilities while avoiding the pitfalls of overfitting to dataset-specific cues.

4.7 Qualitative Results and Discussions

4.7.1 Attention Visualization of the FCG.

In Figure 3, we present a comparative visualization of the affinity maps within the spatial module under two distinct training scenarios: one utilizing FCG and the other lacking it. This juxtaposition sheds light on the variance in response of the affinity map to each query token given these conditions. With the FCG-enhanced model, it is clear that the queries more accurately focus on their respective facial component. However the queries in the model without FCG consistently focus on the same area, predominantly around the lips. This tendency can be attributed to the manipulation type in the FF++, especially the most difficult NT type, which primarily alters lip motion, leading it to concentrate on the lips area in the absence of FCG. This contrast highlights the effectiveness of our strategy in steering the model’s focus towards four pertinent facial parts, thereby reducing the model’s reliance on dataset-specific cues and prevents degradation of its generalization capability.

Towards the Detection of Novel Deepfake Techniques. Beyond comprehensive comparisons of video-based Deepfake detection, we also evaluate the proposed approach with spatial module enabled only on unseen image-based Deepfake detection, particularly focusing on the recent Diffusion models. The results are reported in Table 7. We adhere to the protocol established by prior research and conduct experiments on the CelebA-HQ [14] split of the DiffusionForensics [40]

dataset using our model pre-trained upon FF++ and the off-the-shelf SBI model. Furthermore, We use * to indicate following the settings of [40] to train the models upon images generated by SD-v2 [32] and evaluate against images produced by SD-v2, IF [34], DALLE-2 [30], and Midjourney³. We also show the results of our approach (Ours*) along with CNNDet* [39], F3Net* [28] and DIRE* [40]. The results indicate that our approach significantly enhance capabilities for countering novel generative models in the detection of synthesized face images. We find that the FCG mechanism maximizes the use of the rich semantic encodings from foundational model to focus on detecting artifacts on faces. Furthermore, we compare our method with the SOTA image-based Deepfake detection method SBI [35] in zero-shot evaluation. It’s important to note that both SBI method and ours were trained on the FF++ dataset and evaluated on images generated by novel Deepfake techniques. The outstanding results demonstrate our approach’s ability to adapt to and counter the latest unseen synthetic face generation technologies, underscoring its strong generalizability.

5 Conclusion

In this paper, we introduce a pioneering method that leverages the capabilities of CLIP to detect Deepfake videos through the identification of temporal affinity inconsistencies and spatial artifacts on key facial features. Our approach is inspired by the remarkable successes of CLIP, particularly its exceptional generalization capability. By harnessing facial features extracted from the CLIP image encoder, we effectively guide the learnable side-network decoder away from learning dataset-specific cues with the FCG loss. Through comprehensive experimentation, we affirm the effectiveness of our approach, demonstrating its superiority over state-of-the-art techniques across challenging datasets and highlighting its advantages in scenarios with limited training data.

References

- [1] Chen, L., Zhang, Y., Song, Y., Liu, L., Wang, J.: Self-supervised learning of adversarial example: Towards good generalizations for deepfake detection. In: Conference on Computer Vision and Pattern Recognition (CVPR) (2022)
- [2] Cherti, M., Beaumont, R., Wightman, R., Wortsman, M., Ilharco, G., Gordon, C., Schuhmann, C., Schmidt, L., Jitsev, J.: Reproducible scaling laws for contrastive language-image learning. In: Conference on Computer Vision and Pattern Recognition (CVPR) (2023)
- [3] Das, R., Dukler, Y., Ravichandran, A., Swaminathan, A.: Learning expressive prompting with residuals for vision transformers. In: Conference on Computer Vision and Pattern Recognition (CVPR) (2023)
- [4] deepfake: Deefake. <https://github.com/deepfakes/faceswap/> (2018), accessed: 2023-04-12
- [5] Dolhansky, B., Bitton, J., Pflaum, B., Lu, J., Howes, R., Wang, M., Ferrer, C.C.: The deepfake detection challenge (dfdc) dataset (2020)
- [6] Dosovitskiy, A., Beyer, L., Kolesnikov, A., Weissenborn, D., Zhai, X., Unterthiner, T., Dehghani, M., Minderer, M., Heigold, G., Gelly, S., et al.: An image is worth 16x16 words: Transformers for image recognition at scale. arXiv preprint arXiv:2010.11929 (2020)

³<https://www.midjourney.com>

- [7] Guo, H., Hu, S., Wang, X., Chang, M.C., Lyu, S.: Eyes tell all: Irregular pupil shapes reveal gan-generated faces. In: International Conference on Acoustics, Speech and Signal Processing (ICASSP) (2022)
- [8] Haliassos, A., Mira, R., Petridis, S., Pantic, M.: Leveraging real talking faces via self-supervision for robust forgery detection. In: Conference on Computer Vision and Pattern Recognition (CVPR) (2022)
- [9] Haliassos, A., Vougioukas, K., Petridis, S., Pantic, M.: Lips don't lie: A generalisable and robust approach to face forgery detection. In: Conference on Computer Vision and Pattern Recognition (CVPR) (2021)
- [10] Hu, E.J., Shen, Y., Wallis, P., Allen-Zhu, Z., Li, Y., Wang, S., Wang, L., Chen, W.: LoRA: Low-rank adaptation of large language models. In: International Conference on Learning Representations (ICLR) (2022)
- [11] Jia, M., Tang, L., Chen, B.C., Cardie, C., Belongie, S., Hariharan, B., Lim, S.N.: Visual prompt tuning. European Conference on Computer Vision (ECCV) (2022)
- [12] Jiang, L., Li, R., Wu, W., Qian, C., Loy, C.C.: DeeperForensics-1.0: A large-scale dataset for real-world face forgery detection. In: Conference on Computer Vision and Pattern Recognition (CVPR) (2020)
- [13] Kang, M., Zhu, J.Y., Zhang, R., Park, J., Shechtman, E., Paris, S., Park, T.: Scaling up gans for text-to-image synthesis. In: Conference on Computer Vision and Pattern Recognition (CVPR) (2023)
- [14] Karras, T., Aila, T., Laine, S., Lehtinen, J.: Progressive growing of gans for improved quality, stability, and variation. arXiv preprint arXiv:1710.10196 (2017)
- [15] Karras, T., Aila, T., Laine, S., Lehtinen, J.: Progressive growing of GANs for improved quality, stability, and variation. In: International Conference on Learning Representations (ICCV) (2018)
- [16] Karras, T., Laine, S., Aittala, M., Hellsten, J., Lehtinen, J., Aila, T.: Analyzing and improving the image quality of stylegan (2020)
- [17] Kirillov, A., Mintun, E., Ravi, N., Mao, H., Rolland, C., Gustafson, L., Xiao, T., Whitehead, S., Berg, A.C., Lo, W.Y., Dollár, P., Girshick, R.: Segment anything (2023)
- [18] Kowalski, M.: Faceswap. <https://github.com/MarekKowalski/FaceSwap/> (2018), accessed: 2023-04-12
- [19] Li, L., Bao, J., Yang, H., Chen, D., Wen, F.: Advancing high fidelity identity swapping for forgery detection. In: Proceedings of the IEEE/CVF Conference on Computer Vision and Pattern Recognition. pp. 5074–5083 (2020)
- [20] Li, L., Bao, J., Zhang, T., Yang, H., Chen, D., Wen, F., Guo, B.: Face x-ray for more general face forgery detection. In: Conference on Computer Vision and Pattern Recognition (2020)
- [21] Li, Y., Yang, X., Sun, P., Qi, H., Lyu, S.: Celeb-df: A large-scale challenging dataset for deepfake forensics. In: Conference on Computer Vision and Pattern Recognition (CVPR) (2020)
- [22] Lin, T.Y., Goyal, P., Girshick, R., He, K., Dollár, P.: Focal loss for dense object detection. In: Proceedings of the IEEE International Conference on Computer Vision (ICCV) (Oct 2017)

- [23] Lin, Z., Geng, S., Zhang, R., Gao, P., de Melo, G., Wang, X., Dai, J., Qiao, Y., Li, H.: Frozen clip models are efficient video learners (2022)
- [24] Liu, R., Huang, J., Li, G., Feng, J., Wu, X., Li, T.H.: Revisiting temporal modeling for clip-based image-to-video knowledge transferring. In: Conference on Computer Vision and Pattern Recognition (CVPR) (2023)
- [25] Mengde, X., Zheng, Z., Fangyun, W., Han, H., Xiang, B.: Side adapter network for open-vocabulary semantic segmentation. In: Conference on Computer Vision and Pattern Recognition (CVPR) (2023)
- [26] Nichol, A., Dhariwal, P., Ramesh, A., Shyam, P., Mishkin, P., McGrew, B., Sutskever, I., Chen, M.: Glide: Towards photorealistic image generation and editing with text-guided diffusion models (2022)
- [27] Oquab, M., Darcet, T., Moutakanni, T., Vo, H., Szafraniec, M., Khalidov, V., Fernandez, P., Haziza, D., Massa, F., El-Nouby, A., Assran, M., Ballas, N., Galuba, W., Howes, R., Huang, P.Y., Li, S.W., Misra, I., Rabbat, M., Sharma, V., Synnaeve, G., Xu, H., Jegou, H., Mairal, J., Labatut, P., Joulin, A., Bojanowski, P.: Dinov2: Learning robust visual features without supervision (2023)
- [28] Qian, Y., Yin, G., Sheng, L., Chen, Z., Shao, J.: Thinking in frequency: Face forgery detection by mining frequency-aware clues. In: European Conference on Computer Vision (ECCV) (2020)
- [29] Radford, A., Kim, J.W., Hallacy, C., Ramesh, A., Goh, G., Agarwal, S., Sastry, G., Askell, A., Mishkin, P., Clark, J., et al.: Learning transferable visual models from natural language supervision. In: International Conference on Machine Learning (ICML) (2021)
- [30] Ramesh, A., Dhariwal, P., Nichol, A., Chu, C., Chen, M.: Hierarchical text-conditional image generation with clip latents (2022)
- [31] Rombach, R., Blattmann, A., Lorenz, D., Esser, P., Ommer, B.: High-resolution image synthesis with latent diffusion models. In: Conference on Computer Vision and Pattern Recognition (CVPR) (2022)
- [32] Rombach, R., Blattmann, A., Lorenz, D., Esser, P., Ommer, B.: High-resolution image synthesis with latent diffusion models (2022)
- [33] Rossler, A., Cozzolino, D., Verdoliva, L., Riess, C., Thies, J., Nießner, M.: Faceforensics++: Learning to detect manipulated facial images. In: International Conference on Computer Vision (ICCV) (2019)
- [34] Saharia, C., Chan, W., Saxena, S., Li, L., Whang, J., Denton, E.L., Ghasemipour, K., Gontijo Lopes, R., Karagol Ayan, B., Salimans, T., et al.: Photorealistic text-to-image diffusion models with deep language understanding. arXiv preprint arXiv:2205.11487 **35**, 36479–36494 (2022)
- [35] Shiohara, K., Yamasaki, T.: Detecting deepfakes with self-blended images. In: Conference on Computer Vision and Pattern Recognition (CVPR) (2022)
- [36] Tang, L., Jia, M., Wang, Q., Phoo, C.P., Hariharan, B.: Emergent correspondence from image diffusion (2023)
- [37] Thies, J., Zollhöfer, M., Nießner, M.: Deferred neural rendering: Image synthesis using neural textures. ACM Trans. Graph. (2019)

- [38] Thies, J., Zollhöfer, M., Stamminger, M., Theobalt, C., Nießner, M.: Face2face: Real-time face capture and reenactment of rgb videos. *Commun. ACM* (2018)
- [39] Wang, S.Y., Wang, O., Zhang, R., Owens, A., Efros, A.A.: Cnn-generated images are surprisingly easy to spot... for now. In: *Proceedings of the IEEE Conference on Computer Vision and Pattern Recognition (CVPR)*. pp. 8695–8704 (2020)
- [40] Wang, Z., Bao, J., Zhou, W., Wang, W., Hu, H., Chen, H., Li, H.: Dire for diffusion-generated image detection. In: *Proceedings of the IEEE International Conference on Computer Vision (ICCV)* (2023)
- [41] Wang, Z., Bao, J., Zhou, W., Wang, W., Li, H.: Altfreezing for more general video face forgery detection. In: *Proceedings of the IEEE Conference on Computer Vision and Pattern Recognition (CVPR)*. pp. 4129–4138 (June 2023)
- [42] Xu, Y., Liang, J., Jia, G., Yang, Z., Zhang, Y., He, R.: Tall: Thumbnail layout for deepfake video detection. In: *Proceedings of the IEEE Conference on Computer Vision and Pattern Recognition (CVPR)*. pp. 22658–22668 (2023)
- [43] Zhao, T., Xu, X., Xu, M., Ding, H., Xiong, Y., Xia, W.: Learning self-consistency for deepfake detection. In: *International Conference on Computer Vision (ICCV)* (2021)
- [44] Zheng, Y., Bao, J., Chen, D., Zeng, M., Wen, F.: Exploring temporal coherence for more general video face forgery detection. In: *International Conference on Computer Vision (ICCV)* (2021)
- [45] Zhu, X., Fei, H., Zhang, B., Zhang, T., Zhang, X., Li, S.Z., Lei, Z.: Face forgery detection by 3d decomposition and composition search. *IEEE Transactions on Pattern Analysis and Machine Intelligence* (2023)

Supplementary Materials

6 More Experiments for Model Analysis

In this section, we provide additional evaluation results for the purpose of further model analysis and demonstration for the effectiveness of the proposed approach. We continue to use the Area Under the Receiver Operating Characteristic curve (AUROC) in percentage as the evaluation metric in subsequent experiments.

6.1 Model Performance on Videos with In-the-Wild Faces

Through our extensive research, we observe that prior studies adopt various evaluation protocols for videos containing frames with missing faces. In Section 4.3, following the SBI protocol, we assess videos with identifiable faces normally, while assigning 0.5 as the final prediction score to those with unidentifiable or missing faces. We consider this evaluation approach restrictive, given that real-world videos frequently exhibit dynamic camera movements and shot transitions, potentially resulting in some frames of the videos lacking visible faces.

To provide a more thorough evaluation of our model’s performance in such scenarios, instead of directly setting 0.5 for those challenging videos, we substitute the frames, containing significant facial movements and missing faces, with blank images followed by re-evaluating our model. The updated performance results are presented in Table 8. From results, we observe that our model adeptly handles these challenging videos, demonstrating its robustness to scenarios with missing faces and significant facial movements. Notably, we see marked improvement in performance on the CDF dataset, which is characterized by frequent changes in camera perspectives.

Table 8: **Re-evaluation Incorporating Videos with In-the-Wild Faces:** We report the cross-dataset performance of the model on the dataset including videos with in-the-wild faces. This version of evaluation is denoted with *. Our methods shows significant capability in handling the complexities of real-world videos.

Model	CDF	DFDC	FSh	DFo	Avg.
Xception [33]	73.7	70.9	72.0	84.5	75.3
Face X-ray [20]	79.5	65.5	92.8	86.8	81.2
LipForensics [9]	82.4	73.5	97.1	97.6	87.7
SBI(c23) [35]	<u>92.9</u>	72.0	-	-	-
FTCN [44]	86.9	74.0	98.8	98.8	89.6
RealForensics [8]	86.9	75.9	99.7	99.3	90.5
AltFreezing [41]	89.5	-	<u>99.4</u>	99.3	-
TALL-Swin [42]	90.8	76.8	99.7	99.6	91.7
Ours(ViT-L/14)	92.3	<u>81.2</u>	97.5	<u>99.4</u>	<u>92.6</u>
Ours(ViT-L/14)*	93.9	81.5	98.2	99.6	93.3

6.2 Generalization and Robustness to Diffusion Models

In Table 7, we explore the effectiveness of our method for the novel face generative models (i.e., various Diffusion Models (DMs)). We employ the CelebA-HQ subset from the DiffusionForensics [40] to detect images generated by DMs. This subset comprises 28,000 real images from CelebA-HQ [14] and 42,000 sampled face images produced by the SD-v2 [32] model, which are

prompted with ‘‘A professional photograph of a face.’’ The data from both the real and SD-v2 samples is allocated into three distinct sets: 26,000 for training, 1,000 for validation, and 1,000 for testing. Additionally, the subset includes 1,000 images from IF [34], 500 from DALLE-2 [30], and 100 from Midjourney⁴, specifically reserved for the unseen face-domain evaluation.

Furthermore, in real-world scenarios, images often undergo various post-processing adjustments, making robustness against these unseen perturbations essential. In this context, we assess the robustness of our model against two types of disturbances: Gaussian blur($\sigma = 0, 1, 2, 3$) and JPEG compression($quality = 100, 65, 30$). We explore the robustness of DIRE [40], SBI [35] and our model. We use * to indicate following the settings of [40] to train the models, while the remaining evaluations are conducted in a zero-shot manner. The results are shown in Table 9. Our model continues to exhibit strong evaluation results without significant performance drops against perturbations. This is particularly evident in the zero-shot evaluation, demonstrating robust generalization and resilience.

Table 9: **Image Robustness Evaluation:** We also assess the zero-shot robustness of detection performance, measured in AP(%), across CelebA-HQ [14] split of the DiffusionForensics [40] dataset. * indicates that the detectors have been further trained.

Method	JPEG (Quality)			Blur (Sigma)				Avg.
	100	65	30	0	1	2	3	
SBI [35]	65.2	53.5	56.3	65.2	51.3	52.9	54.2	55.6
Ours	92.2	85.2	79.8	92.2	92.8	91.9	89.7	88.5
DIRE* [40]	100	99.8	99.8	100	99.9	99.9	99.9	99.9
Ours*	100	99.6	99.7	100	99.8	99.7	99.7	99.7

6.3 Model Architecture Comparison

To highlight the superiority of our proposed model architecture, we conduct a comparative analysis with the Efficient Video Learner (EVL) introduced in [23]. EVL employs another side-network video learner that progressively decodes per-layer patch embeddings using traditional attention blocks. Additionally, the patch embeddings undergo several modules before feeding into the self-attention module for enhanced temporal modelling, including a cross-frame attention module, a temporal convolution module, and temporal position encoding. Results of cross-dataset evaluation are detailed in Table 10. The experiments reveal that our model significantly outperforms the EVL across all datasets, particularly with notable performance improvements on the CDF and FSh datasets, where our model outperforms EVL by 6.7% and 5.5%, respectively. Furthermore, our method features significantly fewer trainable parameters compared to the EVL, being ≈ 20 times smaller. This highlights our method’s efficiency in learning temporal inconsistencies in a lightweight framework.

6.4 Effectiveness of Extensive Augmentations for Generalization

In this section, we explore the effects of training augmentations on the generalizability of models. Our analysis presented in Table 11 focuses on the cross-dataset performance of our model trained with extensive data augmentations (color shifting, brightness shifting, blurring, ..., etc.) and with simple augmentations (random resize cropping and random horizontal flipping). For reference, we

⁴<https://www.midjourney.com>

Table 10: **Comparison of Model Architectures:** We compare our model architecture with the Efficient Video Learner (EVL) [23] through cross-dataset evaluation to illustrate the efficacy of our spatial and temporal module decoder design. This design effectively adapts generalizable features from the CLIP image encoder to create a versatile Deepfake detector under a lightweight regime.

Method	# params	CDF	DFDC	FSh	DFo	Avg.
EVL (ViT-L/14)	58.3M	82.1	78.2	90.6	96.1	86.8
Ours (w/o FCG)	250K	<u>88.8</u>	<u>81.2</u>	<u>96.1</u>	<u>99.1</u>	<u>91.3</u>
Ours	250K	92.3	81.2	97.5	99.4	92.6

Table 11: **Generalizability of Models Under Different Augmentations:** We explore the impact of data augmentations on model generalizability by comparing the cross-dataset performance of models trained with and without extensive augmentations. †: The evaluation is conducted using model weights available in the official repository.

Method	CDF	DFDC	FSh	DFo	Avg.
RealForensics	86.9	75.9	99.7	99.3	90.5
RealForensics [†]	79.3	72.7	96.7	99.0	86.9(-3.6)
Ours	92.3	81.2	97.5	99.4	92.6
Ours (w/o ext.)	88.7	81.3	96.2	99.3	91.4(-1.2)

additionally provide the optimal performance metrics for RealForensics, alongside the performance of its counterpart that was trained with basic augmentations (including grayscale conversion, random horizontal flipping, and random resize cropping), which is evaluated using the model weights provided in the official repository. The findings highlight that the RealForensics approach sees a significant average performance reduction of 3.6% when trained with simple training augmentations. However, our proposed method exhibits a much lesser impact, with a mere 1.2% decrease. This contrast emphasizes the efficacy of the features extracted by the CLIP image encoder to improve model generalizability, even in the absence of extensive training augmentations.

6.5 Robustness Evaluation Against Perturbations

To assess the robustness of our model against common perturbations, we adopt the training protocol described in [8], where the model is trained on the FF++ dataset with a limited set of augmentations, specifically random flipping and random resize cropping. We then evaluate the model’s resilience on the FF++ testing subset with various perturbations applied, as suggested by DeeperForensics [12]. These perturbations, varying across five intensity levels, include modifications such as color saturation (CS), color contrast (CC), block-wise occlusions (Block), color component noise (Noise), Gaussian blur (Blur), JPEG compression (JPEG), and video compression (Comp.). We also present the performance of the model trained with augmentations detailed in Section 4.1 to demonstrate the effectiveness of data augmentations against these perturbations. The results are summarized in Table 13. Our method shows comparable performance when trained without extensive augmentations, we further demonstrate the effectiveness of extensive augmentations to improve model robustness to perturbations.

When referring to Table 11, we notice the RealForensics method trained with only simple augmentations is unable to remain its generalizability to unseen datasets, despite its promising performance in the robustness evaluation. We thus surmise previous methods potentially rely on dataset specific artifacts to maintain the saturated robustness performance. Therefore, we follow the same robustness protocol on FF++ and apply perturbations on the CDF dataset, then we evaluate the same

Table 12: **Importance of Facial Components in FCG:** We evaluate the cross-dataset performance on models trained under the FCG excluding specific facial components. This experiment demonstrates the effectiveness of each facial parts to improve model generalization.

Method	CDF	DFDC	FSh	DFo	Avg.
Ours	92.3	<u>81.2</u>	<u>97.5</u>	99.4	92.6
w/o eyes	92.3	82.5	96.2	99.4	92.6
w/o nose	92.3	80.8	97.6	99.4	<u>92.5</u>
w/o lips	92.0	<u>81.2</u>	97.1	99.4	92.4
w/o skin	88.2	81.1	96.0	<u>98.8</u>	91.0

Table 13: **Video Robustness Evaluation:** Following the protocols of prior methods, we train the model on FF++ without extensive augmentations (w/o ext.), using only random horizontal flip and random cropping for augmentation. Subsequently, the model is tested under various perturbations across five intensity levels. The performance metrics of previous methods presented in the table are directly sourced from their respective publications.

Method	Clean	CS	CC	Block	Noise	Blur	JPEG	Comp.	Avg
Xception	99.8	99.3	98.6	<u>99.7</u>	53.8	60.2	74.2	62.1	78.3
Face X-ray	99.8	97.6	88.5	99.1	49.8	63.8	88.6	55.2	77.5
LipForensics	<u>99.9</u>	<u>99.9</u>	<u>99.6</u>	87.4	73.8	<u>96.1</u>	95.6	95.6	92.5
FTCN	99.4	99.4	96.7	97.1	53.1	95.8	98.2	86.4	89.5
RealForensics	99.8	99.8	<u>99.6</u>	98.9	<u>79.7</u>	95.3	<u>98.4</u>	<u>97.6</u>	<u>95.6</u>
TALL-Swin	100.0	100.0	100.0	99.8	85.3	97.6	98.5	98.1	97.1
Ours (w/o ext.)	99.2	96.9	96.7	97.5	76.0	93.2	92.9	91.7	92.1
Ours	99.2	97.2	97.5	98.1	78.6	94.9	93.7	93.4	93.1

models trained on FF++ with limited augmentation on the unseen and perturbed CDF dataset to comprehensively estimate the model’s robustness. The results, showcased in Table 14, underscore our model’s exceptional performance against perturbed samples from unseen sources. With an average performance decline of only 8.1% when assessed on clean samples, our model substantially outperforms RealForensics, which experiences a 15.5% drop in performance. This experiment strongly supports our hypothesis that the robustness of previous methods can potentially rely on dataset-specific cues for promising model robustness.

Table 14: **Video Robustness Evaluation on Unseen Dataset:** We further assess the robustness of our model using the CDF dataset, subjecting it to the same series of perturbations. Our focus is a direct comparison between our model and RealForensics, where neither model has been trained with extensive augmentations (w/o ext.). Additionally, we detail the performance drop induced by each type of perturbation, denoted in **blue**, compared to evaluations conducted on the unperturbed version. The minimal performance decline across each category and on average is emphasized in **bold**. †: This evaluation employs model weights sourced from the official repository.

Method	Clean	CS	CC	Block	Noise	Blur	JPEG	Comp.	Avg
RealForensics†	79.3	71.5	64.8	68.3	58.8	56.6	62.9	63.4	63.8
		(-7.8)	(-14.5)	(-11.0)	(-20.5)	(-22.7)	(-16.4)	(-15.9)	(-15.5)
Ours	88.7	87.7	85.6	88.7	69.2	78.6	80.0	74.2	80.6
(w/o ext.)		(-1.0)	(-2.1)	(-0.0)	(-19.5)	(-10.1)	(-8.7)	(-14.5)	(-8.1)

Algorithm 1 The workflow of the ViT transformer encoder layer given embeddings from the previous layer.

```

1: Input  $x$ 
2: Output  $emb$ 
3:  $\hat{x} \leftarrow LN_1(x)$ 
4:  $q \leftarrow W_Q\hat{x} + B_Q\hat{x}$  ▷ Query Transform
5:  $k \leftarrow W_K\hat{x} + B_K\hat{x}$  ▷ Key Transform
6:  $v \leftarrow W_V\hat{x} + B_V\hat{x}$  ▷ Value Transform
7:  $z \leftarrow \mathbf{MHSA}(q, k, v)$  ▷ Multi-head Self-Attention
8:  $out \leftarrow W_Oz + B_Oz$ 
9:  $x' \leftarrow x + out$ 
10:  $emb \leftarrow x' + MLP(LN_2(x'))$ 

```

6.6 Importance of Facial Components in the FCG

In Table 12, we present the cross-dataset performance of models trained by selectively excluding certain facial components from our Face Component Guidance (FCG) mechanism. We observe that excluding guidance on the ‘eyes’, ‘nose’, and ‘lips’ has a minor effect on the average model performance in terms of cross-dataset generalization. However, a significant decrease occurs when excluding the ‘skin’ facial part. This suggests that the ‘skin’ component is a critical facial feature for generalization, and misguiding the model’s focus can lead to poorer performance than a model trained without any guidance (as shown in Table 2). Given these findings, we opt to include all facial parts in our FCG, as this approach yields superior performance across all datasets.

7 Elaboration of Attention Attribute Extraction

To elucidate the connection between attention attributes and patch embeddings within the Vision Transformer (ViT) encoder pipeline, we detail the workflow of a typical ViT encoder layer in Algorithm 1. Each layer accepts embeddings from the preceding layer as input, which encompasses a class embedding along with numerous patch embeddings. These embeddings are then processed through a self-attention mechanism to produce output embeddings for the subsequent layer. Initially, the class embedding is represented by a learnable token, and patch embeddings are formed by a distinct patch extraction layer given an image (for further details, please see the ViT paper [6]). In the algorithm presented, W_s and B_s , for $s \in \{Q, K, V, O\}$, signify the weights and biases associated with the linear transformations. LN_1 and LN_2 represent the layer normalization modules. The **MHSA** stands for the Multi-Head Self-Attention mechanism, which operates on the query, key, and value embeddings of the class and patch tokens. Furthermore, the *MLP* (multi-layer perceptron) includes two linear layers and a GeLU activation layer. The attention attributes $\mathcal{A}_{l,\gamma}$, where $\gamma \in \{q, k, v\}$, are extracted as specified in the cited lines 4, 5, and 6, and the extracted patch embeddings \mathcal{P}_l are referred to in line 10.